On the structure and dynamics of sheared and rotating turbulence: Direct numerical simulation and wavelet-based coherent vortex extraction

Frank G. Jacobitz,[1,2] Lukas Liechtenstein,[2] Kai Schneider,[2] and Marie Farge[3]
[1]*Mechanical Engineering Program, University of San Diego, 5998 Alcalá Park, San Diego, California 92110, USA*
[2]*Laboratoire de Modélisation et Simulation Numérique en Mécanique du Centre National de la Recherche Scientifique, Université de Provence, 39 rue Joliot-Curie, 13453 Marseille Cedex 13, France*
[3]*Laboratoire de Météorologie Dynamique du Centre National de la Recherche Scientifique, Ecole Normale Supérieure, 24 rue Lhomond, 75231 Paris Cedex 5, France*

(Received 11 September 2007; accepted 12 February 2008; published online 8 April 2008)

The influence of rotation on the structure and dynamics of sheared turbulence is investigated using a series of direct numerical simulations. Five cases are considered: turbulent shear flow without rotation, with moderate rotation, and with strong rotation, where the rotation configuration is either parallel or antiparallel. For moderate rotation rates an antiparallel configuration increases the growth of the turbulent kinetic energy, while the parallel case reduces the growth as compared to the nonrotating case. For strong rotation rates decay of the energy is observed, linear effects dominate the flow, and the vorticity probability density functions tend to become Gaussian. Visualizations of vorticity show that the inclination angle of the vortical structures depends on the rotation rate and orientation. Coherent vortex extraction, based on the orthogonal wavelet decomposition of vorticity, is applied to split the flow into coherent and incoherent parts. It was found that the coherent part preserves the vortical structures using only a few percent of the degrees of freedom. The incoherent part was found to be structureless and of mainly dissipative nature. With increasing rotation rates, the number of wavelet modes representing the coherent vortices decreases, indicating an increased coherency of the flow. Restarting the direct numerical simulation with the filtered fields confirms that the coherent component preserves the temporal dynamics of the total flow, while the incoherent component is of dissipative nature. © *2008 American Institute of Physics*.
[DOI: 10.1063/1.2896284]

I. INTRODUCTION

Shear and rotation affect the structure formation and dynamics of turbulent flows. This study considers turbulence with uniform vertical shear $S=\partial U/\partial y$ and constant system rotation $f=2\Omega$. The rotation axis is perpendicular to the plane of shear, and a schematic of the geometry is shown in Fig. 1. In such a flow two main configurations are possible: system rotation can be parallel or antiparallel to the vorticity of the mean shear. Theoretical investigations have shown that the parallel case always has a stabilizing effect, while the antiparallel case has a destabilizing effect for low rotation rates and is again stabilizing for high rotation rates.[1,2]

These results are confirmed by a comprehensive study by Brethouwer.[3] In this work, the results from direct numerical simulations (DNS) are compared with computations based on rapid distortion theory (RDT). In order to obtain conditions similar to those in the high shear region of a turbulent boundary layer, the simulations are characterized by a high shear rate. Such high shear rates lead to the predominance of linear effects and make a comparison with RDT possible. Further theoretical RDT results have been presented in Refs. 4 and 5.

Simple shear flows have been considered in many previous studies. For example, stratified shear flows have been studied using DNS by Gerz *et al.*[6] Holt *et al.*[7] as well as Jacobitz *et al.*[8] Schumann and Gerz[9] used stratified shear flows to estimate turbulent mixing with applications in atmospheric turbulence. Itsweire *et al.*[10] considered anisotropy properties of such flows and show that estimates of the dissipation rate ϵ, based on oceanographic measurements of a few components, may be poor. Miesch[11] related the simulation results of Holt *et al.*,[7] Jacobitz,[12] and others to large-scale processes in the convection zone and tachocline on the sun.

Wavelet techniques have been introduced in the early nineties to analyze turbulent flows.[13,14] Since then different directions for wavelets and turbulence have been exploited, e.g., signal processing approaches, interpretations in the multifractal community, cospectra, analysis, and eduction of coherent structures using experimental data.

In Refs. 15 and 16 the coherent vortex simulation (CVS) approach has been introduced to compute and to model turbulent flows. Further developments have been presented in Refs. 17–19. The idea of CVS is to combine nonlinear approximation with denoising and, additionally, to exploit the properties of wavelets for numerical analysis. Wavelets yield attractive discretizations for operator equations. They allow autoadaptive discretizations by estimating the local regularity of the solution. Furthermore, many integral and differential operators have a sparse representation in a wavelet basis and can furthermore efficiently be preconditioned using diagonal scaling. For a review, we refer to the book of

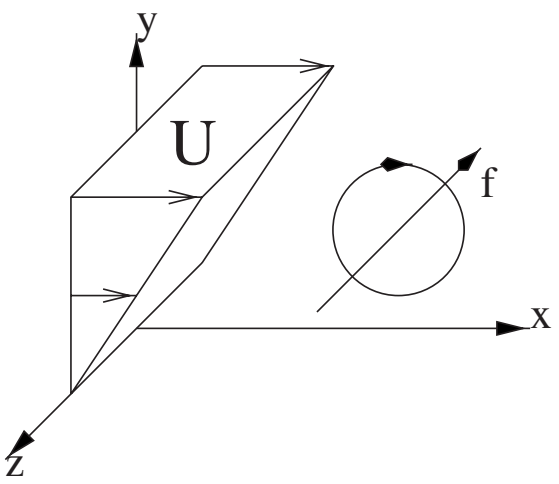

FIG. 1. Schematic of the flow configuration with uniform vertical shear $S=\partial U/\partial y$ and rotation $f=2\ \Omega$. Note that this schematic shows a parallel configuration with negative rotation ratio f/S.

Cohen.[20] The idea of CVS is based on filtering turbulent flows using adaptive multiresolution techniques. Therewith the flow is split into two parts, a coherent flow, whose evolution is deterministically computed in an adaptive basis, and an incoherent flow, which is noiselike and whose effect on the coherent flow is modeled.

The aim of the paper is twofold. First, we study structure formation and the fully nonlinear dynamics of uniformly sheared and rotating turbulence. Hence a series of DNS is performed with a lower shear rate compared to a previous study of this flow.[3] Second, to check the potential of CVS, we apply coherent vortex extraction (CVE) to the DNS data. Using a variety of analysis tools, such as low-order and higher-order statistics, spectra, probability density functions, and volume visualization, we aim to both validate the applicability of the CVE approach as well as collect information about the physics of turbulence in rotating shear flows.

In the next section, the flow configuration, the direct numerical simulation method, and the wavelet-based coherent vortex extraction are introduced. In Sec. III, first the temporal evolution of the simulations based on the transport equation for turbulent kinetic energy is presented and the influence of the magnitude and orientation of the rotation ratio f/S is investigated. Then, we apply CVE to the DNS data and thus split the total flow into coherent and incoherent contributions at a fixed instant in time. The structure of the coherent and incoherent fields is discussed by visualization of vorticity, the corresponding properties of the spectral transport equation of energy, and higher-order statistics. The dynamics of the coherent and incoherent components is investigated by advancing the filtered and unfiltered flow fields in time using DNS. Finally, conclusions of the present work are presented.

II. NUMERICAL APPROACH: DNS AND CVE

This section describes the flow configuration, introduces the direct numerical simulation approach, and summarizes the coherent vortex extraction method.

A. Flow configuration

This study considers turbulence in a rotating shear flow. A schematic of the flow is shown in Fig. 1 and the following coordinates $\boldsymbol{x}=(x,y,z)=(x_1,x_2,x_3)$ are used: The x-axis of the coordinate system denotes the downstream direction, the y-axis the vertical direction, and the z-axis the spanwise direction. The mean flow $\boldsymbol{U}=(Sy,0,0)$ is unidirectional in the downstream direction and has a constant shear $S=\partial U/\partial y$ in the vertical direction. In the case of a positive shear rate this mean flow results in a negative mean vorticity in the spanwise direction. The system rotation $\boldsymbol{\Omega}=(0,\Omega,0)$, with Coriolis parameter $f=2\Omega$, is directed in the positive spanwise direction and therefore perpendicular to the plane of shear. For positive values of the rotation ratio f/S the system rotation axis is antiparallel to the mean vorticity generated by the mean flow with uniform shear. For negative values of f/S the axes are parallel. Note that due to our choice of a different coordinate system the sign of the rotation ratio f/S is inverted compared to Brethouwer.[3] However, the meaning of parallel and antiparallel configurations remains the same.

B. Direct numerical simulations

This work is based on the continuity equation for incompressible flow and the Navier–Stokes equations with a Coriolis term. A geostrophic balance is assumed to preserve the mean shear. The following equations are obtained for the fluctuating velocities $\boldsymbol{u}=(u,v,w)=(u_1,u_2,u_3)$:

$$\nabla\cdot\boldsymbol{u}=0, \tag{1}$$

$$\frac{\partial\boldsymbol{u}}{\partial t}+\boldsymbol{u}\cdot\nabla\boldsymbol{u}+Sx_2\frac{\partial\boldsymbol{u}}{\partial x_1}+Su_2\boldsymbol{e}_1+2\boldsymbol{\Omega}\times\boldsymbol{u}=-\frac{1}{\rho_0}\nabla p+\nu\nabla^2\boldsymbol{u}. \tag{2}$$

Here p contains the pressure and centrifugal force, ρ_0 is the density, ν is the kinematic viscosity, and $\boldsymbol{e}_1$ is the unit vector in the downstream direction.

Following Rogallo,[21] the equations of motion are solved in a reference frame moving with the mean flow and periodic boundary conditions can be applied to the fluctuating quantities. The resulting equations of motion in the moving coordinate system can be found in Jacobitz *et al.*[8] The spatial discretization is accomplished using a classical Fourier collocation method, and the simulations are advanced in time with a fourth-order embedded Runge–Kutta scheme.[22] Regridding is used periodically to prevent an ongoing distortion of the numerical grid and aliasing errors are controlled. The simulation code has been validated for turbulent stratified shear flows in Jacobitz *et al.*[8] against previous results reported by Holt *et al.*[7] All simulations are performed on a computational grid of size $2\pi\times2\pi\times2\pi$ with $256\times256\times256$ grid points.

The initial velocity field is obtained from a separate simulation of isotropic turbulence with a maximum in the energy spectrum at wave number $k=13$. The initial values of the Taylor-microscale Reynolds number $\mathrm{Re}_\lambda=q\lambda/\nu=56$ and the shear number $SK/\epsilon=2$ are fixed, but these values evolve as the simulations progress in time. Here $K=\overline{u_iu_i}/2$ is the

TABLE I. Properties of the simulations at nondimensional time $St=5$.

Case	Configuration	Re_λ	SK/ϵ
$f/S=0$	Shear only	72.15	4.817
$f/S=+0.5$	Antiparallel	100.43	6.036
$f/S=-0.5$	Parallel	42.52	4.094
$f/S=+5$	Antiparallel	35.49	5.901
$f/S=-5$	Parallel	37.22	5.846

turbulent kinetic energy, $q=\sqrt{2K}$ an isotropic fluctuating velocity scale, $\epsilon=\nu\overline{\partial u_i/\partial x_k \partial u_i/\partial x_k}$ the dissipation rate, and $\lambda=\sqrt{5\nu q^2/\epsilon}$ an isotropic Taylor microscale. Due to the low initial value of the shear number an equilibrium state is obtained in the nonrotating case. Due to the isotropic initial conditions, an initial decrease of the Reynolds number to values $\mathrm{Re}_\lambda<45$ is observed before shear or rotation effects determine its further evolution. This choice is different from the previous work by Brethouwer.[3] His work is characterized by a high initial value of the shear number $SK/\epsilon=18$ to resemble the conditions in a high shear region of a turbulent boundary layer. The high shear rate prevents an initial decay of the turbulent kinetic energy, and the initial value of the Reynolds number $\mathrm{Re}_\lambda=39$ is chosen to be lower. Note that a different definition of the Reynolds number and Taylor microscale is used, where our Re_λ is equal to $\sqrt{1.5}\mathrm{Re}_\lambda$ of the previous study.[3] A more detailed discussion of shear number effects in turbulent nonrotating stratified shear flows can be found in Jacobitz and Sarkar[23] and Shih *et al.*.[24]

The rotation number f/S is varied and five cases are considered here with $f/S=0$, for nonrotating shear flow, $f/S=\pm 0.5$, for moderate rotation, and $f/S=\pm 5$, for strong rotation. A positive sign of f/S corresponds to an antiparallel configuration and a negative sign to a parallel one. Properties of the simulations are given in Table I. Four more cases with $f/S=\pm 1$ and $f/S=\pm 10$ have been computed but are not discussed here in detail to simplify the discussion.

C. Wavelet-based coherent vortex extraction

In many turbulent flows coherent structures are observed which seem to be imbedded in a random background sea. Hence, the aspect of denoising may allow to eliminate the noise in a given flow realization, and the remaining part can then be called and defined as coherent structures. In Refs. 15 and 25, a wavelet-based method to extract coherent vortices out of both two- and three-dimensional turbulent flows was proposed, which is motivated by denoising. The idea is to apply the orthogonal wavelet decomposition to the vorticity field $\boldsymbol{\omega}$ at a given time instant t with resolution $N=2^{3J}=256^3$.

In the following we first fix the notation for the wavelet decomposition of a three-dimensional vector field and summarize the main ideas of wavelet-based coherent vortex extraction. For more details on the orthogonal wavelet transform, or its extension to higher dimensions, we refer the reader to textbooks, e.g., Ref. 26, for more details on the coherent vortex extraction method we refer to the original papers.

We consider a vector field $\boldsymbol{u}(\boldsymbol{x})$ for $\boldsymbol{x}\in[0,2\pi]^3$ and decompose it into an orthogonal wavelet series

$$\boldsymbol{u}(\boldsymbol{x})=\sum_{\lambda\in\Lambda}\tilde{\boldsymbol{u}}_\lambda\psi_\lambda(\boldsymbol{x}), \tag{3}$$

where the multi-index $\lambda=(j,i_x,i_y,i_z,d)$ denotes the scale j, the position $\boldsymbol{i}=(i_x,i_y,i_z)$, and the seven directions $d=1,\ldots,7$ of the wavelets. The corresponding index set Λ is

$$\Lambda=\{\lambda=(j,i_x,i_y,i_z,d), j=0,\ldots,J-1; i_x,i_y,i_z=0,\ldots,2^j-1 \text{ and } d=1,\ldots,7\}. \tag{4}$$

Due to orthogonality the coefficients are given $\tilde{\boldsymbol{u}}_\lambda=\langle\boldsymbol{u},\psi_\lambda\rangle$ where $\langle\cdot,\cdot\rangle$ denotes the L^2-inner product, defined by $\langle f,g\rangle=\int_{[0,2\pi]^3}f(\boldsymbol{x})g(\boldsymbol{x})d\boldsymbol{x}$. The coefficients measure the fluctuations of $\boldsymbol{u}$ around scale 2^{-j} and around position $\boldsymbol{i}/2^j$ in one of the seven possible directions. The fast wavelet transform[26] yields an efficient algorithm to compute the N wavelet coefficients $\tilde{\boldsymbol{u}}_\lambda$ from the N grid point values of $\boldsymbol{u}$ and has linear complexity. In the current paper we have chosen the Coiflet 30 wavelet, which has ten vanishing moments and is well appropriated to represent the current flow simulations.

The idea of the coherent vortex extraction method can be summarized in the following three step procedure.

- *Decomposition:* compute the wavelet coefficients of vorticity $\tilde{\boldsymbol{\omega}}_\lambda$ using the fast wavelet transform.
- *Thresholding:* apply the thresholding function ρ_ε to the wavelet coefficients $\tilde{\boldsymbol{\omega}}_\lambda$, thus reducing the relative importance of the coefficients with small absolute value.
- *Reconstruction:* reconstruct the coherent vorticity $\boldsymbol{\omega}_C$ from the thresholded wavelet coefficients using the fast inverse wavelet transform. The incoherent vorticity $\boldsymbol{\omega}_I$ is obtained by simple subtraction, $\boldsymbol{\omega}_I=\boldsymbol{\omega}-\boldsymbol{\omega}_C$.

The thresholding function ρ corresponds to

$$\rho_\varepsilon(a)=\begin{cases}a & \text{if } |a|>\varepsilon\\ 0 & \text{if } |a|\leqslant\varepsilon,\end{cases} \tag{5}$$

where ε denotes the threshold.

The thresholding parameter ε depends on the variance of the incoherent vorticity σ_n and on the sample size N. The threshold

$$\varepsilon_D=\sigma_n\sqrt{2\ln N} \tag{6}$$

is motivated from denoising theory.[27] However, the variance of the incoherent vorticity is unknown and has to be estimated from the available total vorticity $\boldsymbol{\omega}$. As a first guess we take the variance of the total vorticity, which overestimates the variance of the incoherent vorticity. Therewith we split the field into coherent and incoherent parts and then take the variance of the incoherent vorticity as a new improved estimator. In Ref. 28 we have developed an iterative algorithm for this task, based on the method presented in Ref. 15. Here we decided to perform one iteration step only which can be justified by the fast convergence of the iterative

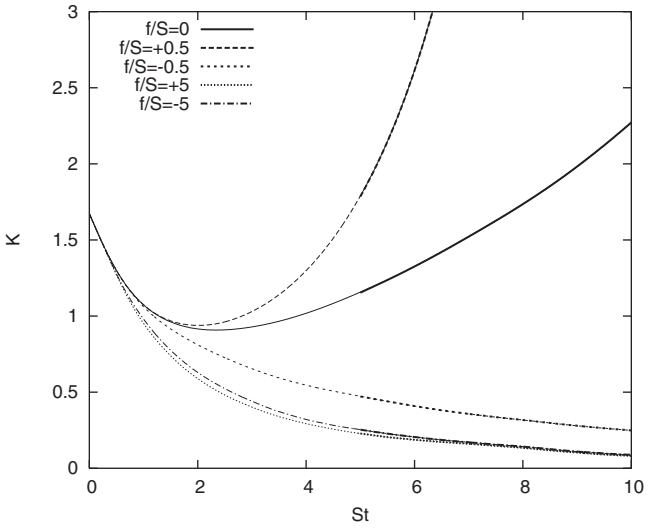

FIG. 2. Evolution of the turbulent kinetic energy K with nondimensional time St. The thin lines correspond to the evolution of the total flow and the thick lines correspond to the evolution of the coherent flows started after CVE at $St=5$.

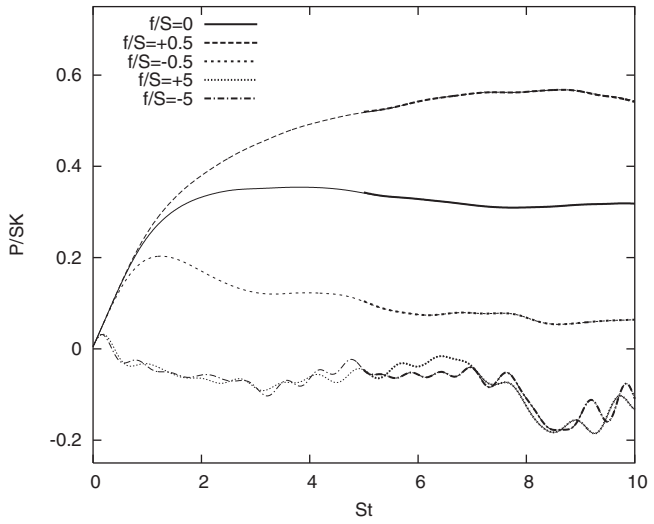

FIG. 3. Evolution of the normalized production rate P/SK with nondimensional time St. The thin lines correspond to the evolution of the total flow and the thick lines correspond to the evolution of the coherent flows started after CVE at $St=5$.

procedure and by the fact that the computational effort is minimized.

With the above algorithm the flow is split into two parts: a coherent flow, corresponding to the coherent vortices, and an incoherent flow, corresponding to the background noise.[15] This decomposition yields $\boldsymbol{\omega}=\boldsymbol{\omega}_C+\boldsymbol{\omega}_I$. Due to orthogonality we have $\langle\boldsymbol{\omega}_C,\boldsymbol{\omega}_I\rangle=0$, and hence it follows that enstrophy is conserved, i.e., $Z=Z_C+Z_I$, where $Z=\frac{1}{2}\langle\boldsymbol{\omega},\boldsymbol{\omega}\rangle$. Inverting the curl operator we obtain the corresponding velocity fields, i.e., $\boldsymbol{v}=\boldsymbol{v}_C+\boldsymbol{v}_I$. As the Biot–Savart operator is not diagonal in wavelet space for the decomposition of the turbulent kinetic energy, we have $K=K_C+K_I+\epsilon$, where ϵ is small (cf. Ref. 15) and with $K=\frac{1}{2}\langle\boldsymbol{u},\boldsymbol{u}\rangle$.

III. RESULTS

In this section, the evolution of the turbulent kinetic energy K is discussed first. Then the decomposition of the flow into coherent and incoherent contributions is studied. Different analysis methods, such as volume visualization, spectra, and probability density functions, are used to evaluate both the properties of the decomposition as well as the physics of turbulence in rotating shear flows. Finally, the dynamics of the flow is investigated by advancing the total, coherent, and incoherent components in time using DNS.

A. Evolution of the turbulent kinetic energy

The evolution of the turbulent kinetic energy K in nondimensional time St is shown in Fig. 2. All five cases have an initial decay of the turbulent kinetic energy due to the isotropic initial conditions. The nonrotating case with $f/S=0$ develops shear production of turbulence at about $St=2$ and eventually shows an exponential growth of the turbulent kinetic energy. The moderately rotating cases, with $f/S=\pm 0.5$, exhibit different behaviors. The antiparallel configuration, with $f/S=+0.5$, shows the strongest eventual growth of K, while the parallel configuration, with $f/S=-0.5$, leads to a decay. The strongly rotating cases with $f/S=\pm 5$, however, both result in a strong decay of the turbulent kinetic energy. These findings are consistent with previous theoretical work[1,2] and direct numerical simulations.[3]

To obtain insight into the process of the turbulent kinetic energy evolution, a nondimensional form of the transport equation of K is considered,

$$\gamma=\frac{1}{SK}\frac{dK}{dt}=\frac{P}{SK}-\frac{\epsilon}{SK}. \tag{7}$$

Here $P=-S\overline{u_1u_2}$ is the production rate, $\epsilon=2\nu Z$ the viscous dissipation rate, and γ the growth rate of the turbulent kinetic energy.

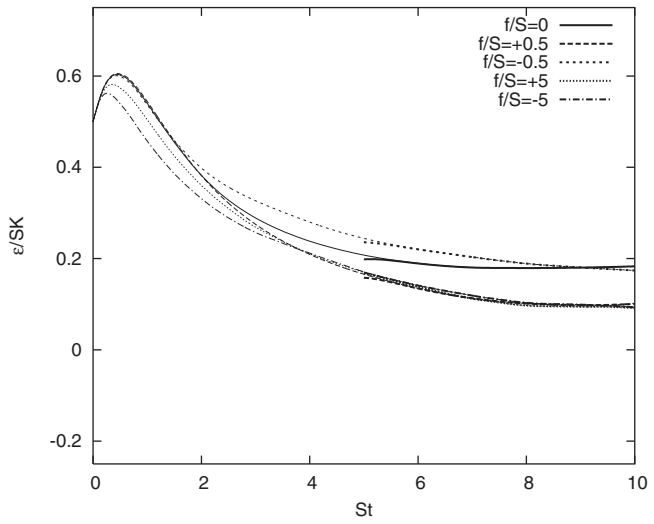

FIG. 4. Evolution of the normalized dissipation rate ϵ/SK with nondimensional time St. The thin lines correspond to the evolution of the total flow and the thick lines correspond to the evolution of the coherent flows started after CVE at $St=5$.

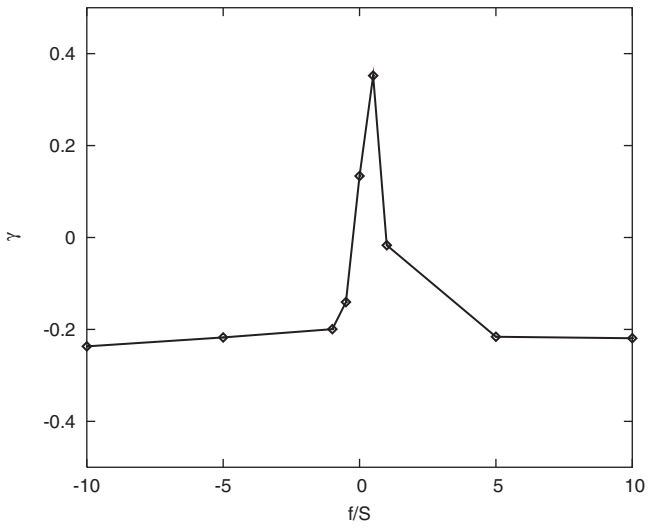

FIG. 5. Dependence of the growth rate γ of the turbulent kinetic energy on the rotation ratio f/S at nondimensional time $St=5$.

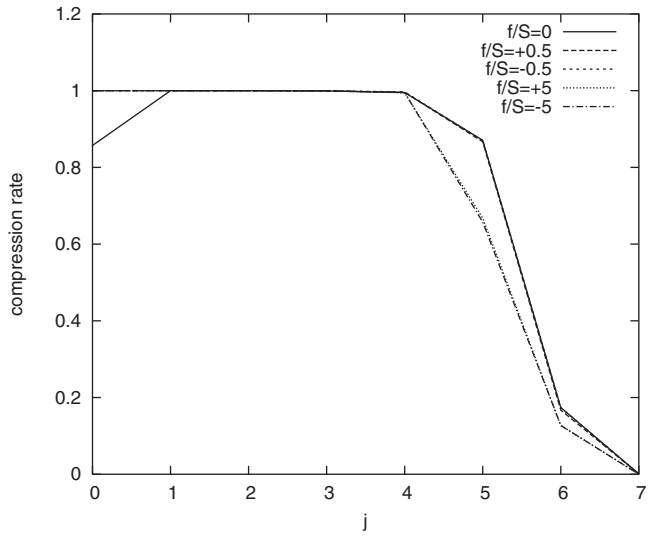

FIG. 6. Dependence of the fraction of retained wavelet coefficients on the scale index j for different rotation rates f/S.

The two right-hand-side terms are shown in Figs. 3 and 4, respectively. The results for the nonrotating case with $f/S=0$ agree well with previous results: Both the normalized production P/SK and normalized dissipation ϵ/SK reach asymptotic states. The normalized production $P/SK=-2b_{12}=0.32$ assumes negative two times the generally reported value for the off-diagonal component of the Reynolds shear stress anisotropy tensor $b_{12}=\overline{u_1u_2}/\overline{u_iu_i}=-0.16$. Similarly, the shear number $SK/\epsilon=5.5$, which is the inverse of the normalized dissipation rate, assumes a typical value.

The increased kinetic energy growth in the moderately rotating case with $f/S=+0.5$ is due to a strong increase of the normalized production rate P/SK as well as a decrease of the normalized dissipation rate ϵ/SK, as compared to the nonrotating case with $f/S=0$. The decay of the kinetic energy in the moderately rotating case with $f/S=-0.5$ is due to a decrease of the normalized production rate and an unchanged normalized dissipation rate, as compared to the nonrotating case. In the strongly rotating cases with $f/S=\pm 5$, the normalized production rate P/SK has collapsed and the turbulent kinetic energy growth is diminished.

The dependence of the growth rate γ of the turbulent kinetic energy on the rotation ratio f/S is shown in Fig. 5 for nondimensional time $St=5$. Positive values of the growth rate correspond to growth of the turbulent kinetic energy, while negative values are obtained for decay of the turbulent kinetic energy. The results show a narrow regime of growth with a sharp maximum growth rate for $f/S=+0.5$. These observations again are in accordance with previous theoretical work[1,2] and also with direct numerical simulations.[3]

B. Coherent vortex extraction

The CVE method has been applied to the vorticity field of the five cases at nondimensional time $St=5$. This time was chosen far enough in the simulations such that shear and rotation effects are developed. The total vorticity $\boldsymbol{\omega}_{\text{tot}}$ is decomposed into a coherent vorticity $\boldsymbol{\omega}_{\text{coh}}$ and an incoherent vorticity $\boldsymbol{\omega}_{\text{inc}}$. The results of the decomposition are shown in Table II.

The percentage of wavelet modes used to represent the coherent component of the vorticity field, a measure for the compression rate, decreases from 3.388% for $f/S=0$ to 3.312% for $f/S=+0.5$ (3.347 for $f/S=-0.5$) and then to 2.504% for $f/S=5$ (2.486% for $f/S=-5$). Therefore, in the latter case, only 420×10^3 modes instead of 16.8×10^6 modes are used to represent the coherent part of the flow field. Note that the above compression rates would correspond to Fourier cutoff wavenumbers of only $k_c=41$ and $k_c=37$ using low-pass filtering.

To gain further insight we now consider the percentage of retained wavelet coefficients at different scale indices j. The scale index j is related to a mean wavenumber $k_j=k_02^j$, where k_0 is the centroid wavenumber of the chosen

TABLE II. Properties of the decomposition of the total fields into coherent and incoherent components.

Case	Compression rate	Z_{tot}	Z_{coh} (%)	Z_{inc} (%)	K_{tot}	K_{coh} (%)	K_{inc} (%)
$f/S=0$	3.388	117.33	95.95	4.046	0.771 54	99.69	0.1527
$f/S=+0.5$	3.312	144.76	95.88	4.124	1.192 8	99.76	0.1231
$f/S=-0.5$	3.347	56.423	96.85	3.148	0.315 31	99.69	0.1487
$f/S=+5$	2.504	18.914	99.10	0.9058	0.152 36	99.91	0.0384
$f/S=-5$	2.486	21.202	99.20	0.7967	0.169 19	99.91	0.0350

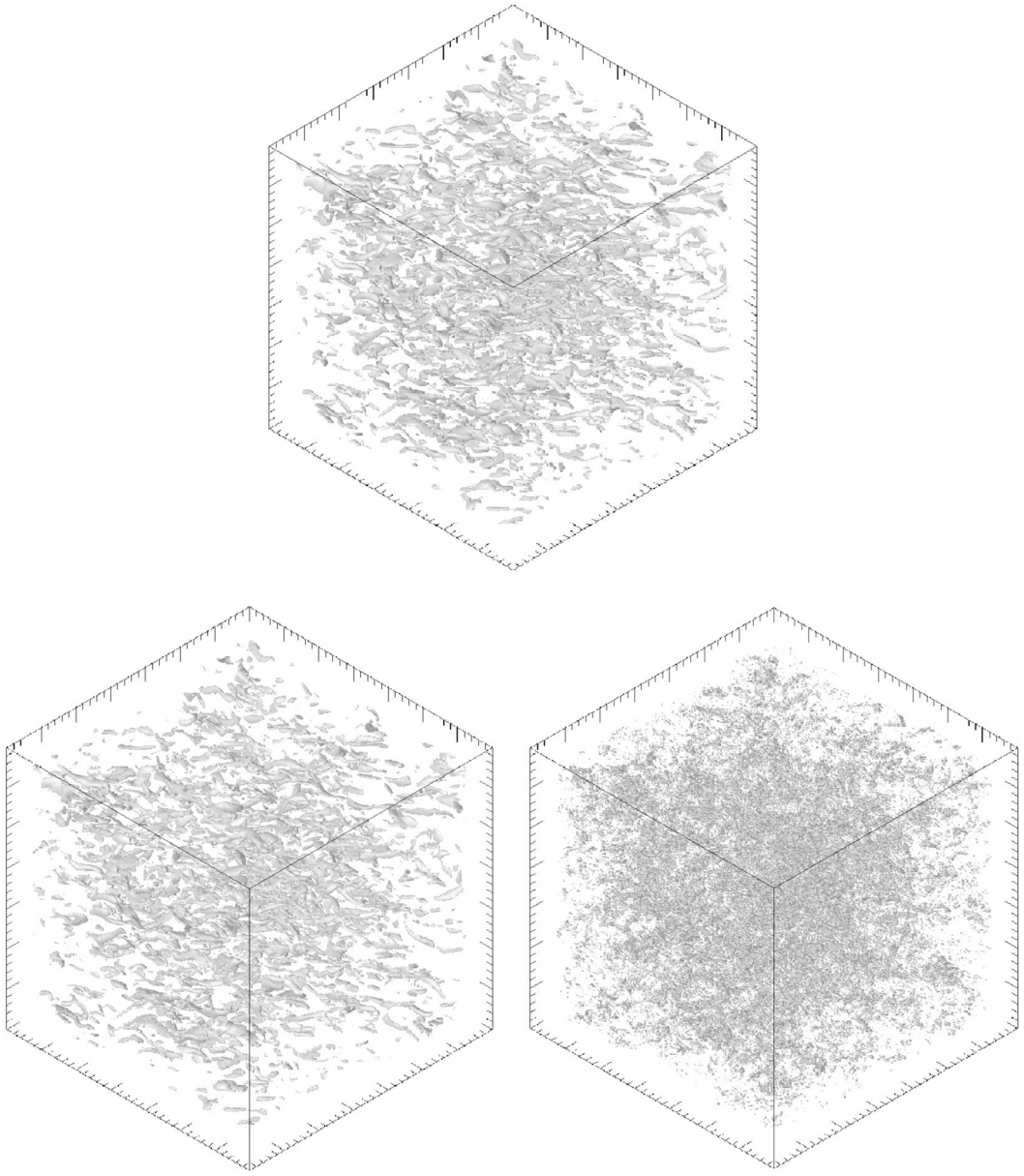

FIG. 7. Isosurfaces of total (top), coherent (bottom left), and incoherent (bottom right) vorticities at nondimensional time $St=5$ for the antiparallel $f/S=0.5$ case. The isosurfaces are shown in an isometric view. The values of the isosurfaces are $|\boldsymbol{\omega}|=4\sigma_{\mathrm{tot}}$ for the total and coherent vorticities and $4\sigma_{\mathrm{inc}}\approx\frac{4}{5}\sigma_{\mathrm{tot}}$ for the incoherent one.

wavelet.[13] The wavelet representation implies that there are 7×2^{3j} wavelet coefficients at a given scale j. Figure 6 shows the fraction of retained wavelet coefficients on the scale index j for different rotation rates f/S. At large scales, i.e., for $j\leqslant 4$, almost all coefficients are retained and correspond to the coherent part. At smaller scales, where the total number of coefficients vastly increases, the fraction of retained coefficients decreases strongly. This effect is more pronounced for rapidly rotating flows.

Despite an increase of the compression rate with increasing f/S, the energy contained in the coherent component increases from 99.69% to 99.9%, for both parallel and antiparallel configurations (see Table II). Hence, virtually all of the turbulent kinetic energy is retained in the coherent component. The enstrophy contained in the coherent component increases dramatically from 95.95% to 99.20%. This indicates that the coherency of the flow increases with increasing rotation, which holds for both parallel and antiparallel configurations.

C. Volume visualization

Figure 7 shows isosurfaces of vorticity at nondimensional time $St=5$ for the moderate rotation case, with $f/S=+0.5$. The total vorticity (top) is characterized by well developed vortical structures, and these structures are retained in the coherent field (bottom left). In contrast, the incoherent field (bottom right) contains no organized vortical structures and resembles noise with low amplitude. However, noise is only present in regions of active turbulence. Therefore, quiescent regions remain quiescent in the incoherent fields, as the sum of coherent and incoherent fields must yield the

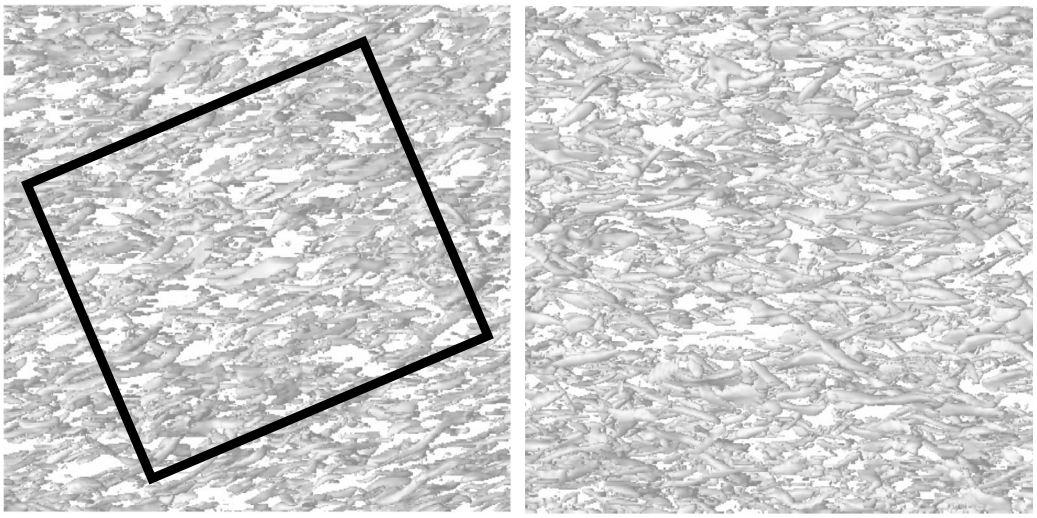

FIG. 8. Isosurfaces of coherent vorticity $|\boldsymbol{\omega}|=4\sigma_{\mathrm{tot}}$. Shear without rotation, $f/S=0$. Front view, x-y plane (left) and top view, x-z plane (right). The black rectangle has an inclination angle $\alpha=23°$.

total. The same observation has been made for the other four cases, with $f/S=0$, $f/S=-0.5$, and $f/S=\pm 5$. We will therefore restrict the visualization of the other cases to the coherent vorticity only.

Note that the isovalues of the total and coherent part are identical, corresponding to four times the standard deviation of the total vorticity, while the isovalue of the incoherent component is chosen as four times the standard deviation of the incoherent part, and it is about a factor of 5 smaller than the above value. Those values were chosen to effectively represent the spatial features of the total, coherent, and incoherent parts.

In order to investigate the effect of shear and rotation on the turbulence structure, we show front and top views of the vorticity field for the five cases with $f/S=0$ (Fig. 8), $f/S=+0.5,+5$ (Fig. 9), and $f/S=-0.5,-5$ (Fig. 10). The front views (x-y plane) in the left columns illustrate the effect of shear and rotation. In all cases the vortical structures are inclined in the y-direction by an angle α to the x-direction. The angle is observed to be dependent on both the magnitude and the sign of the rotation ratio f/S. As a visual aid a black box inclined at the angle α has been added to the figures.

The dependence on the angle α on the rotation ratio f/S is given in Fig. 11. The largest angle $\alpha=25°$ is found for the antiparallel $f/S=+0.5$ case, which also was observed to have the strongest turbulence growth. For both the parallel and antiparallel cases, an increase of the rotation ratio f/S leads to a decrease of the observed angle α. For a given magnitude of the rotation ratio, the angle is always smaller for the parallel configurations. There is a striking similarity between the dependence of the growth rate γ (Fig. 5) and the dependence of the inclination angle α (Fig. 11) on the rotation ratio f/S. For both graphs, there is a sharp increase to the maximum values as the rotation ratio is increased from $f/S=-10$ to $f/S=+0.5$. A further increase from $f/S=+0.5$ to $f/S=+10$, however, results in a more gradual decrease of both quantities. We conjecture that the inclination angle of vortical structures is directly related to the turbulent kinetic energy evolution.

In addition, with increasing rotation ratio, the vortical structures also become more pronounced and exhibit a stronger alignment, resulting in a sparser appearance of structures.

The top views (x-z plane) in the right column of Figs. 8–10 show the vortical structures aligned with the downstream direction. In the strongly rotating cases, the vortical structures are flatter and somewhat resemble structures found in stratified flows. Salhi[4] pointed out similarities between rotation and stratification effects in homogeneous shear flow using RDT.

D. Spectra

The spectral distribution of the total, coherent, and incoherent turbulent kinetic energies is compared in Fig. 12 at nondimensional time $St=5$ for the moderately rotating case with $f/S=+0.5$. The spectra of the total and coherent fields coincide up to a wave number $k\approx 30$, and a faster decay of the spectrum is observed for the coherent field in the dissipative range with wave numbers $k>30$. The spectrum of the incoherent field contains contributions at all wave numbers but is significant only in the dissipative range.

More understanding of the flow dynamics can be gained from the spectral transport equation

$$\frac{dE(k)}{dt}=P(k)+T(k)+\epsilon(k). \tag{8}$$

The different terms of the right hand side of the spectral transport equation are shown in Fig. 13, for the total and coherent flows. The production term $P(k)$ adds energy to the smallest wavenumber modes of the flow. The spectral energy transfer term $T(k)$ redistributes energy from small wave numbers to large wave numbers. Finally, the dissipation term $\epsilon(k)$ removes energy from the modes. The results for the total

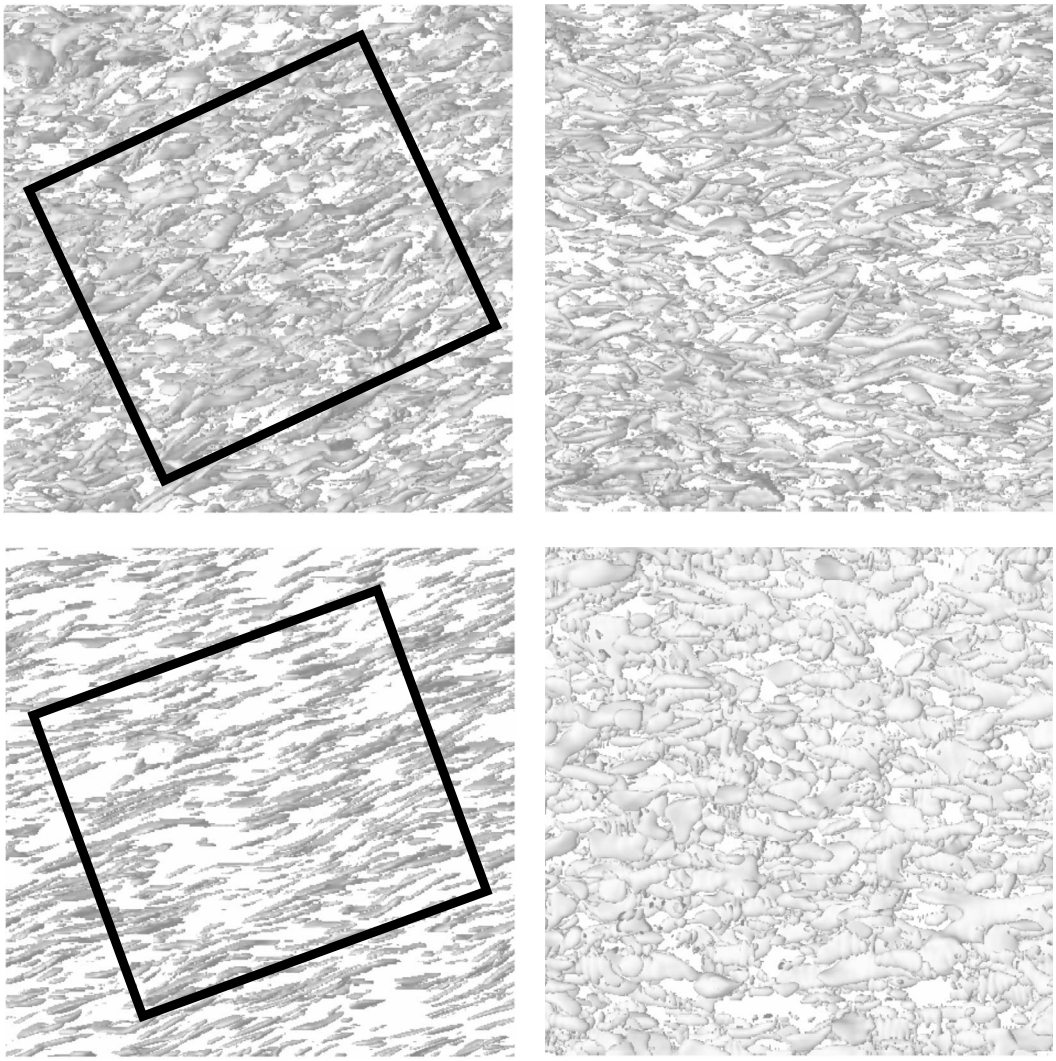

FIG. 9. Isosurfaces of coherent vorticity $|\boldsymbol{\omega}|=4\sigma_{\text{tot}}$. Antiparallel rotation with $f/S=+0.5$ (top) and $f/S=+5$ (bottom). Front views (left) and top views (right). The black rectangles have an inclination angle $\alpha=25°$ (top) and $\alpha=20°$ (bottom).

and coherent flows are identical for the production term $P(k)$ and show only slight differences for the transfer term $T(k)$ for wave numbers of $25<k<35$ and for the dissipation term $\epsilon(k)$ for wave numbers $k>35$. The results suggest that the nonlinear transfer is fully retained by the coherent flow.

The corresponding spectral transport terms for the incoherent flow are shown in Fig. 14. Their character is mainly of dissipative nature. The transfer term almost vanishes across all wave numbers. The production term remains small and is nonzero only for wave numbers much larger than those observed for the total or coherent contributions. The dissipation term, already reduced by a factor of 10 in the figure for comparison purposes, is much larger than the production or transfer terms and contributes almost equally for a wavenumber range of $40<k<80$.

E. Probability density functions

A study of the probability density functions (PDFs) of velocity or vorticity yields information about the higher order statistics of the flow. The PDF of total, coherent, and incoherent velocities is shown in Fig. 15 for the antiparallel configuration, with $f/S=+0.5$. The findings for total and coherent velocity are almost identical and only slightly differ from a Gaussian distribution. The incoherent velocity almost perfectly follows a Gaussian distribution. The PDFs of total, coherent, and incoherent vorticities are shown in Fig. 16 for the antiparallel configuration with $f/S=+0.5$. The results for total and coherent vorticities are again almost identical but they have exponential tails. The incoherent vorticity has a strongly reduced variance and it has also exponential tails.

To obtain insight into the geometrical statistics of the different flow components we consider the relative helicity, which is defined as follows:

$$h=\frac{\boldsymbol{u}\cdot\boldsymbol{\omega}}{\|\boldsymbol{u}\|\,\|\boldsymbol{\omega}\|}. \tag{9}$$

The helicity corresponds to the cosine of the angle between velocity and vorticity. It hence permits us to distinguish between helical structures (swirling motion) for which h has values of ±1 and that correspond to alignment or antialignment of vorticity and velocity, respectively. Two dimensionalization of the flow, i.e., vorticity is perpendicular to veloc-

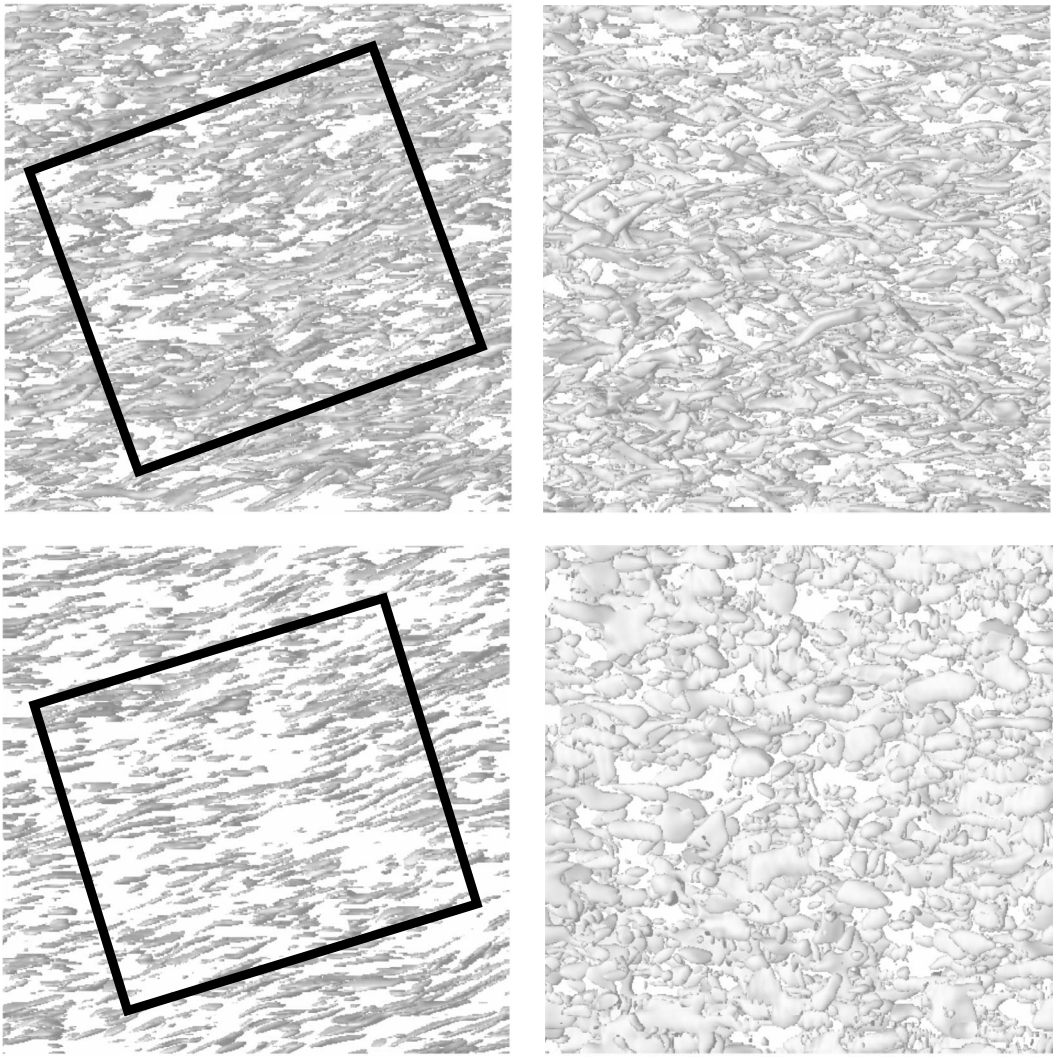

FIG. 10. Isosurfaces of coherent vorticity $|\boldsymbol{\omega}|=4\sigma_{\text{tot}}$. Parallel rotation with $f/S=-0.5$ (top) and $f/S=-5$ (bottom). Front views (left) and top views (right). The black rectangles have an inclination angle $\alpha=20°$ (top) and $\alpha=17°$ (bottom).

ity, results in $h=0$. The PDF of relative helicity is plotted in Fig. 17 for the total, coherent, and incoherent flows for the antiparallel configuration, with $f/S=+0.5$. The PDFs of total and coherent flow superimpose perfectly and exhibit a maximum at $h=0$, which shows two dimensionalization of the flow due to rotation. In contrast the PDF of the incoherent flow is almost flat and shows no preferred alignment, which confirms the noiselike character of the incoherent part.

Figure 18 shows the PDF of the coherent vorticity for the five cases, with no rotation, moderate rotation, and strong rotation, for both parallel and antiparallel configurations. An exponential decay of the PDFs is found for the simulations with no rotation and with moderate rotation. The variance is increased for $f/S=+0.5$ and decreased for $f/S=-0.5$ with respect to the nonrotating case $f/S=0$. For the cases with strong rotation, the PDFs of the coherent vorticity tend toward a Gaussian distribution, indicating that linear processes increasingly dominate the evolution of the flow. This is reflected in the decrease of the flatness, from about 5 for the nonrotating and moderately rotating cases, down to about 3.7 for the strongly rotating cases (see Table III). The skewness of the nonrotating case is negative, about −0.2, and a similar value is observed for $f/S=-0.5$. A moderate rotation in the antiparallel configuration changes the skewness to about −0.14. Strong rotation in the parallel configurations yields a similar value of about −0.13, while the antiparallel case shows a slightly positive value of about 0.087.

F. Evolution of DNS versus CVE

The previous analyses of vorticity structures, energy spectra and spectral transfer, and higher-order statistics suggest that the dynamical information of the total field is retained by the coherent field. It can be anticipated that a temporal integration of the coherent field will result in an evolution similar to that of the total flow field. For the incoherent flow field a viscous decay of the fluctuations can be anticipated.

To better understand the effect of the CVE filtering on the dynamics of the flow, the coherent and incoherent flows have been advanced in time using the DNS code, as was previously done for two-dimensional turbulence in Ref. 29

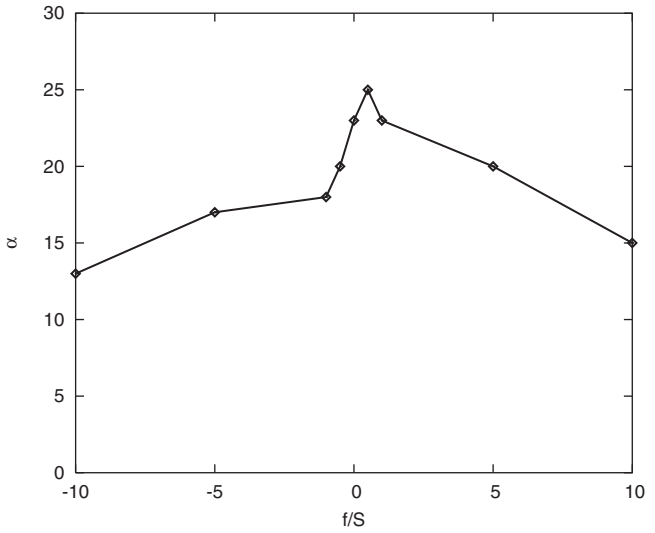

FIG. 11. Dependence of the inclination angle α of the vortical structures to the downstream direction on the rotation ratio f/S.

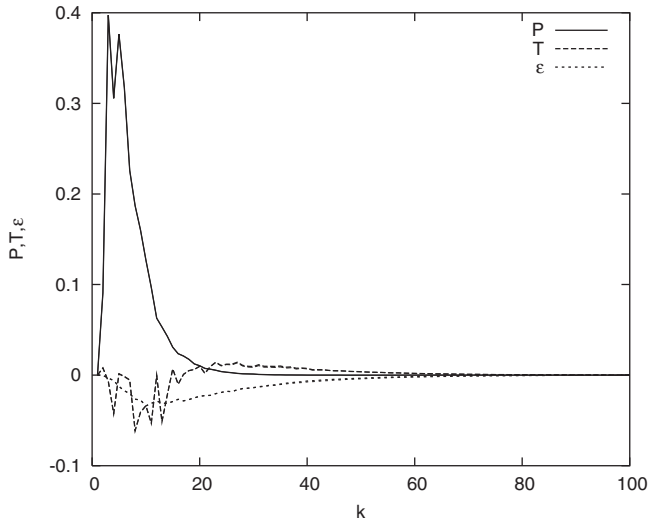

FIG. 13. Spectral transport terms for total and coherent velocity at $St=5$ and for $f/S=+0.5$. Note that the graphs of total and coherent terms almost perfectly coincide.

and for three-dimensional mixing layers in Ref. 30. The evolution of the coherent fields is then compared to the evolution of the original DNS simulation. This will yield additional information about their dynamical behavior. At nondimensional time $St=5$ the total vorticity field is computed from the total velocity field and then decomposed into coherent and incoherent components, as discussed in the previous section. The corresponding coherent and incoherent velocity fields are reconstructed using the Biot–Savart law, and original total and computed coherent and incoherent fields are then advanced using the DNS code to a final nondimensional time $St=10$.

The evolution of the turbulent kinetic energy K of the total and coherent flows is shown in Fig. 2, for the nonrotating, moderately rotating, and strongly rotating cases. The evolution of the total field is shown as a thin line from the initial nondimensional time $St=0$ to the final nondimensional time $St=10$. Note that its evolution remains unaffected by CVE at nondimensional time $St=5$. The evolution of the coherent field is shown as a thicker line from the time of decomposition $St=5$ to the same final nondimensional time $St=10$. In all the five cases the evolution of the total and coherent fields cannot be distinguished. Similarly, the evolution of the total and coherent normalized production rates is identical, as shown in Fig. 3.

The corresponding total and coherent normalized dissipation rates are shown in Fig. 4. Immediately after the decomposition performed at time $St=5$, a small reduction is visible in the coherent field for the nonrotating and the two moderately rotating cases. This reduction is due to the CVE filtering of the vorticity field which has discarded the incoherent component. This leads to a loss of enstrophy which is,

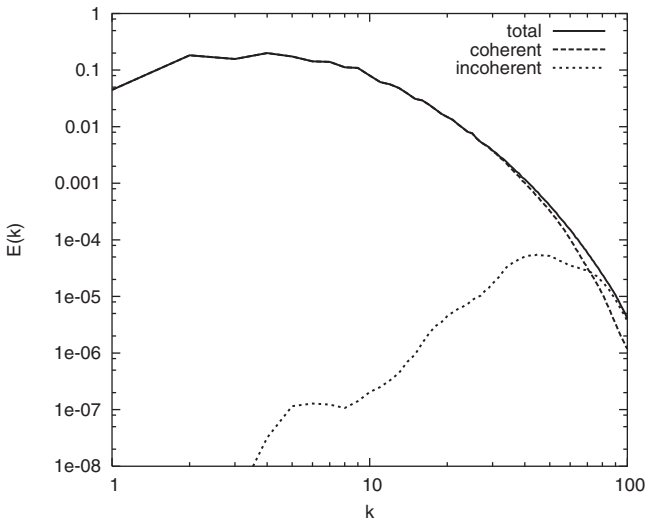

FIG. 12. Spectra of total, coherent, and incoherent velocities at $St=5$ and for $f/S=+0.5$.

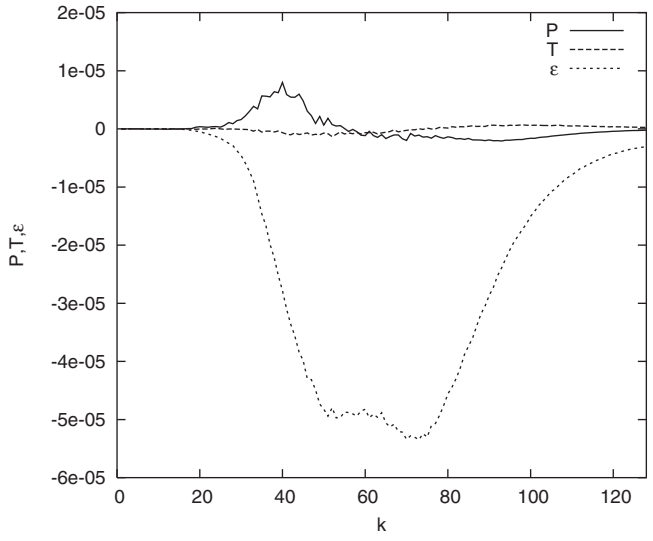

FIG. 14. Spectral transport terms for incoherent velocity at $St=5$ and for $f/S=+0.5$. The dissipation term is shown an order of magnitude smaller to facilitate comparison.

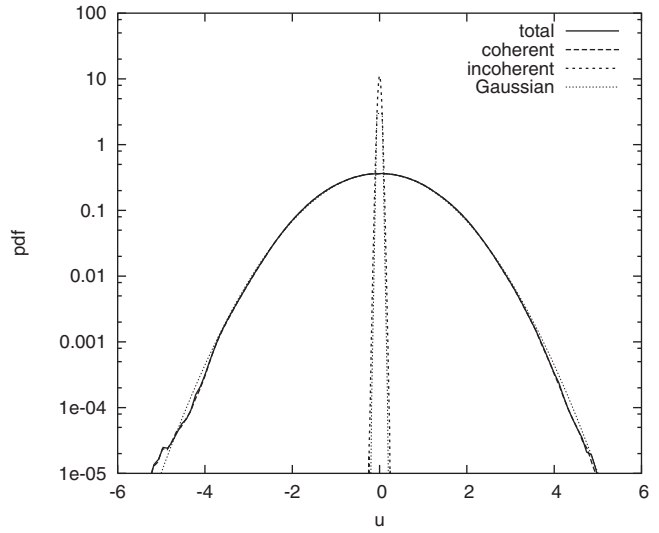

FIG. 15. PDF of total, coherent, and incoherent velocities at $St=5$ and for $f/S=+0.5$.

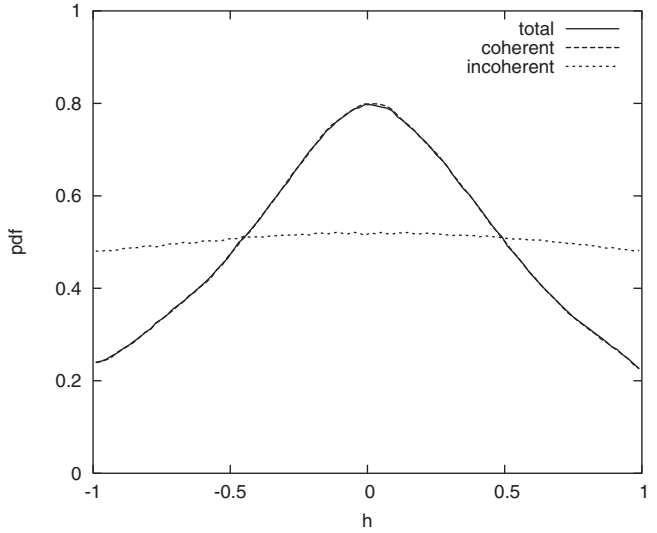

FIG. 17. PDF of relative helicity for total, coherent, and incoherent flows at $St=5$ and for $f/S=+0.5$.

for incompressible flow, directly proportional to dissipation by twice the viscosity. This difference is rapidly recovered within less than one-half nondimensional St time. The simulations demonstrate that the nonlinear dynamics of rotating and sheared turbulence is preserved by the coherent component with only a small number of modes.

The corresponding incoherent terms are several orders of magnitude smaller and are hence shown in separate figures. The evolution of the turbulent kinetic energy of the incoherent part is shown in Fig. 19. Depending on the coherence of the original velocity fields, increasing coherence with increasing f/S, different levels of energy are found in the incoherent flows at the time of decomposition $St=5$. Despite a shear forcing, all five cases show a strong decay with advancing nondimensional time St.

Figures 20 and 21 show the evolution of the normalized production rate P/SK and normalized dissipation rate ϵ/SK of the incoherent flows, respectively. The production term adds a slight amount of energy to the incoherent flows. Note that the terms are normalized with the decaying turbulent kinetic energy of the incoherent fields. The dissipation rate however, is about an order of magnitude larger and dissipates the existing energy far more quickly, except in the antiparallel case $f/S=+0.5$, where the production slightly increases toward the end of the simulation. This effect is due to the starting self-organization of the initially incoherent flow into developing coherent vortices. These results confirm that the incoherent flows are of mainly dissipative nature.

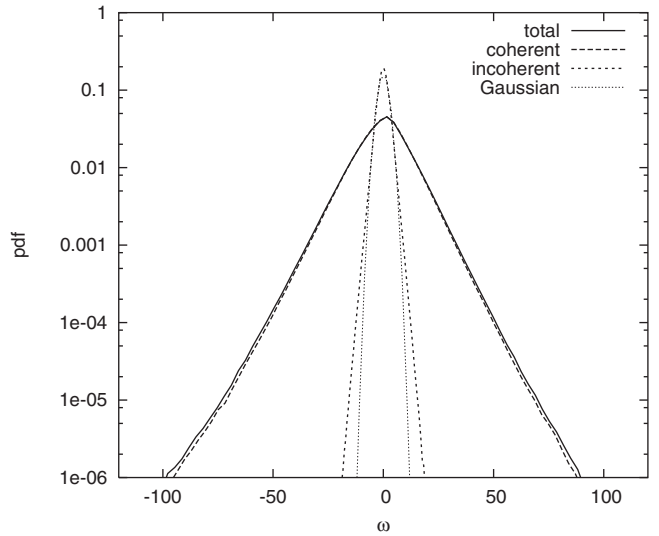

FIG. 16. PDF of total, coherent, and incoherent vorticities at $St=5$ and for $f/S=+0.5$.

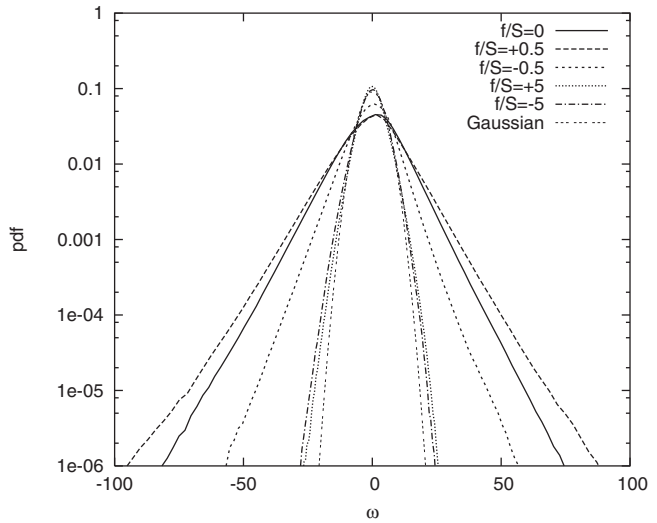

FIG. 18. PDF of coherent vorticity at $St=5$ for $f/S=0$, $f/S=\pm 0.5$, and $f/S=\pm 5$.

TABLE III. Skewness and flatness of vorticity.

Case	S_{tot}	S_{coh}	S_{inc}	F_{tot}	F_{coh}	F_{inc}
$f/S=0$	−0.204 20	−0.194 35	−0.006 471 6	4.9044	4.8390	4.4171
$f/S=+0.5$	−0.138 84	−0.137 07	−0.001 286 6	5.3510	5.2931	4.4290
$f/S=-0.5$	−0.200 65	−0.190 57	−0.002 917 3	4.7304	4.7081	4.3182
$f/S=+5$	0.087 479	0.082 019	0.009 280 4	3.8930	3.8739	5.0335
$f/S=-5$	−0.131 36	−0.125 19	−0.007 125 4	3.6380	3.6252	5.0071

IV. CONCLUSIONS

A series of direct numerical simulations of turbulence in the presence of rotation and shear has been performed in order to gain a more complete understanding of processes in such flows. Five cases are considered: turbulent shear flow without rotation, with moderate rotation, and with strong rotation, where the rotation configuration is either parallel or antiparallel. The evolution of integral quantities illustrates the influence of rotation on the flow dynamics. It was observed that moderate rotation in the antiparallel configuration leads to an increased growth of the turbulent kinetic energy compared to the nonrotating case. Strong rotation, however, results in a rapid decay of turbulent kinetic energy. These findings are consistent with previous theoretical[1,2] and numerical studies.[3] As no rotation term appears in the transport equation for the turbulent kinetic energy, its main impact is on the turbulence production term. Higher-order statistics show that strong rotation suppresses nonlinearity, the vorticity PDFs tend to become Gaussian and decay is observed.

A wavelet-based coherent vortex extraction method was applied to rotating and sheared turbulence simulations for the first time. This method allows for an efficient extraction and analysis of vortical structures contained in such flows. It was found that few (2.5%–3.4%) wavelet coefficients represent the coherent vortices of the flow. This is an excellent compression rate and even better than for isotropic turbulence at the same resolution.[25] For increasing rotation rate, the number of retained wavelet coefficients decreases which confirms the higher coherency of the flow.

Flow visualizations of the coherent vorticity illustrate the different flow topologies for different rotation rates. In the presence of nonlinearity, for the nonrotating and moderately rotating cases, there is interaction between vortical structures themselves. This leads to distortion and scrambling of the structures, and hence to turbulent mixing. When rotation is strong, nonlinearity is inhibited, and we observe elongated structures produced by strain. Mutual interaction is then insignificant and turbulent mixing is reduced.

The vortical structures are observed to be inclined in the vertical direction with respect to the downstream direction. The inclination angle depends on both the magnitude and orientation of the rotation ratio. This dependence of the inclination angle on the rotation ratio mirrors the dependence of the growth rate of the turbulent kinetic energy on the rotation ratio. Both quantities assume a maximum for the antiparallel case with $f/S=+0.5$. We conjecture that the inclination of vortical structures determines the fate of the turbulence.

In order to characterize the dynamics of the coherent and incoherent flows, the production, transfer, and dissipation terms of the spectral transport equation are analyzed. Shear production is only active in the coherent flow and far less

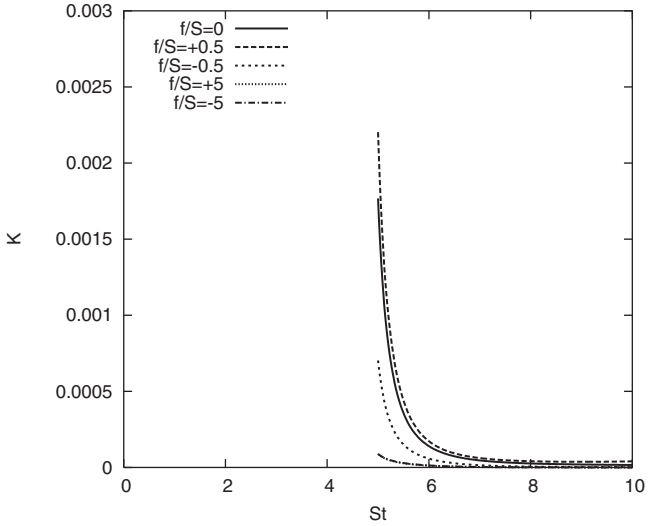

FIG. 19. Evolution of the incoherent turbulent kinetic energy K_{inc} with nondimensional time St.

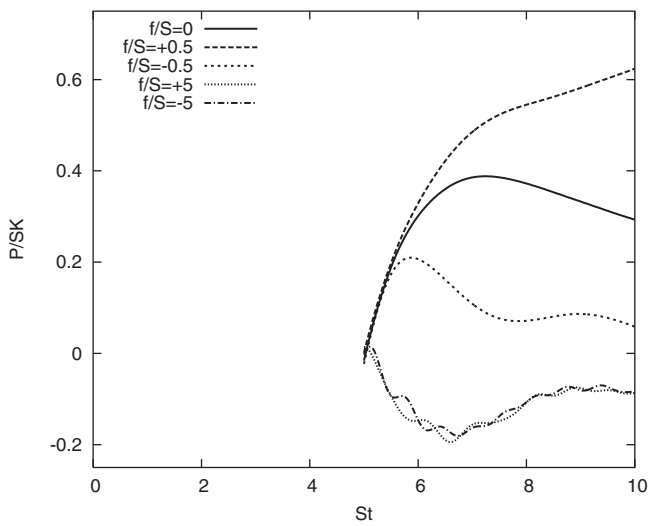

FIG. 20. Evolution of the normalized incoherent production rate P_{inc}/SK with nondimensional time St.

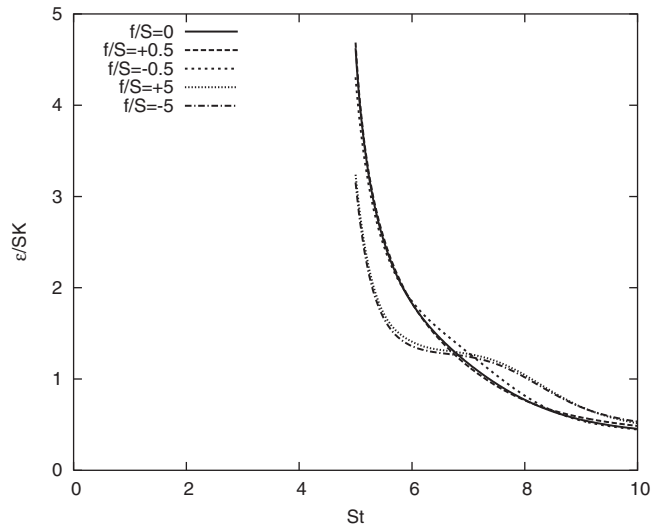

FIG. 21. Evolution of the normalized incoherent dissipation rate $\epsilon_{\mathrm{inc}}/SK$ with nondimensional time St.

important in the incoherent flows. Similarly, spectral transfer occurs only in the coherent flow. Viscous dissipation is present in both the coherent and incoherent flows. The spectral transport terms suggest that the dynamics of coherent and incoherent components are decoupled. The coherent vortices are responsible for the nonlinear dynamics of the flow and determine the future evolution of the flows. The incoherent part is of dissipative nature and can be modeled as turbulent diffusion.

Restarting the DNS with either the total, coherent, and incoherent fields confirms these conjectures. The retained wavelet coefficients to represent the coherent flow correspond to an adaptively refined sparse grid positioned at the centers of the retained wavelet coefficients. The understanding of the structure of the refined grid could lead to an improved predictability of turbulent flows using far fewer degrees of freedom. The results presented here motivate coherent vortex simulations of rotating and sheared turbulence. First results of such an approach for three-dimensional mixing layers are presented in Ref. 30 and are promising.

ACKNOWLEDGMENTS

F.G.J. acknowledges support from the Centre National de la Recherche Scientifique, Department ST2I, and an International Opportunity Grant from the University of San Diego. M.F., L.L., and K.S. acknowledge financial support from the Agence Nationale de la Recherche Grant No. M2TFP. M.F., K.S., and F.G.J. thank the Ahlers Center for International Business of the University of San Diego.

[1] P. Bradshaw, "The analogy between streamline curvature and buoyancy in turbulent shear flow," J. Fluid Mech. **36**, 177 (1969).
[2] D. J. Tritton, "Stabilization and destabilization of turbulent shear-flow in a rotating fluid," J. Fluid Mech. **241**, 503 (1992).
[3] G. Brethouwer, "The effect of rotation on rapidly sheared homogeneous turbulence and passive scalar transport. Linear theory and direct numerical simulations," J. Fluid Mech. **542**, 305 (2005).
[4] A. Salhi, "Similarities between rotation and stratification effects on homogeneous shear flow," Theor. Comput. Fluid Dyn. **15**, 339 (2002).
[5] A. Salhi and C. Cambon, "Advances in rapid distortion theory: from rotating shear flows to the baroclinic instability," J. Appl. Mech. **73**, 449 (2006).
[6] T. Gerz, U. Schumann, and S. E. Elghobashi, "Direct numerical simulation of stratified homogeneous turbulent shear flows," J. Fluid Mech. **200**, 563 (1989).
[7] S. E. Holt, J. R. Koseff, and J. H. Ferziger, "A numerical study of the evolution and structure of homogeneous stably stratified sheared turbulence," J. Fluid Mech. **237**, 499 (1992).
[8] F. G. Jacobitz, S. Sarkar, and C. W. Van Atta, "Direct numerical simulations of the turbulence evolution in a uniformly sheared and stably stratified flow," J. Fluid Mech. **342**, 231 (1997).
[9] U. Schumann and T. Gerz, "Turbulent mixing in stably stratified shear flows," J. Appl. Meteorol. **34**, 33 (1995).
[10] E. C. Itsweire, J. R. Koseff, D. A. Briggs, and J. H. Ferziger, "Turbulence in stratified shear flows: Implications for interpreting shear-induced mixing in the ocean," J. Phys. Oceanogr. **23**, 1508 (1993).
[11] M. S. Miesch, http://www.livingreviews.org/lrsp-2005-1 (2005).
[12] F. G. Jacobitz, "A comparison of the turbulence evolution in a stratified fluid with vertical or horizontal shear," J. Turbul. **2**, 55 (2002).
[13] M. Farge, "Wavelet transforms and their applications to turbulence," Annu. Rev. Fluid Mech. **24**, 395 (1992).
[14] C. Meneveau, "Analysis of turbulence in the orthonormal wavelet representation," J. Fluid Mech. **232**, 469 (1991).
[15] M. Farge, K. Schneider, and N. Kevlahan, "Non-Gaussianity and coherent vortex simulation for two-dimensional turbulence using an adaptive orthonormal wavelet basis," Phys. Fluids **11**, 2187 (1999).
[16] M. Farge and K. Schneider, "Coherent vortex simulation (CVS), a semi-deterministic turbulence model using wavelets," Flow, Turbul. Combust. **66**, 393 (2001).
[17] M. Farge, G. Pellegrino, K. Schneider, A. Wray, and B. Rogallo, "Coherent vortex extraction in three-dimensional homogeneous turbulence: Comparison between CVS-wavelet and POD-Fourier decompositions," Phys. Fluids **15**, 2886 (2003).
[18] D. E. Goldstein and O. V. Vasilyev, "Stochastic coherent adaptive large eddy simulation method," Phys. Fluids **16**, 2497 (2004).
[19] N. Okamoto, K. Yoshimatsu, K. Schneider, M. Farge, and Y. Kaneda, "Coherent vortices in high resolution direct numerical simulation of homogeneous, isotropic turbulence: A wavelet viewpoint," Phys. Fluids **19**, 115109 (2007).
[20] A. Cohen, in *Handbook of Numerical Analysis*, edited by P. G. Ciarlet and J. L. Lions (Elsevier, Amsterdam, 2000), Vol. 7.
[21] R. S. Rogallo, "Numerical experiments in homogeneous turbulence," NASA Report No. TM 81315 (1981).
[22] C. Canuto, M. Y. Hussaini, A. Quarteroni, and T. A. Zang, *Spectral Methods in Fluid Dynamics* (Springer-Verlag, Berlin, 1988).
[23] F. G. Jacobitz and S. Sarkar, "On the shear number effect in stratified shear flow," Theor. Comput. Fluid Dyn. **13**, 171 (1999).
[24] L. H. Shih, J. R. Koseff, J. H. Ferziger, and C. R. Rehmann, "Scaling and parameterization of stratified homogeneous turbulent shear flow," J. Fluid Mech. **412**, 1 (2000).
[25] M. Farge, G. Pellegrino, and K. Schneider, "Coherent vortex extraction in 3D turbulent flows using orthogonal wavelets," Phys. Rev. Lett. **87**, 054501 (2001).
[26] I. Daubechies, *Ten Lectures on Wavelets* (SIAM, Philadelphia, 1992).
[27] D. Donoho and I. Johnstone, "Ideal spatial adaptation via wavelet shrinkage," Biometrika **81**, 425 (1994).
[28] A. Azzalini, M. Farge, and K. Schneider, "Nonlinear wavelet thresholding: A recursive method to determine the optimal denoising threshold," Appl. Comput. Harmon. Anal. **18**, 177 (2005).
[29] M. Farge, G. Goirand, Y. Meyer, F. Pascal, and M. V. Wickerhauser, "Improved predictability of two-dimensional turbulent flows using wavelet packet compression," Fluid Dyn. Res. **10**, 229 (1992).
[30] K. Schneider, M. Farge, G. Pellegrino, and M. Rogers, "Coherent vortex simulation of three-dimensional turbulent mixing layers using orthogonal wavelets," J. Fluid Mech. **534**, 39 (2005).